THE JOURNAL OF PHYSICAL CHEMISTRY C

Subscriber access provided by McMaster University Library

C: Energy Conversion and Storage; Energy and Charge Transport

Operando Mapping of Li Concentration Profiles and Phase Transformations in Graphite Electrodes by MRI and NMR

Sergey A. Krachkovskiy, Jamie M Foster, Jonathan David Bazak, Bruce J. Balcom, and Gillian R. Goward

J. Phys. Chem. C, **Just Accepted Manuscript** • DOI: 10.1021/acs.jpcc.8b06563 • Publication Date (Web): 24 Aug 2018

Downloaded from http://pubs.acs.org on August 27, 2018

Just Accepted

"Just Accepted" manuscripts have been peer-reviewed and accepted for publication. They are posted online prior to technical editing, formatting for publication and author proofing. The American Chemical Society provides "Just Accepted" as a service to the research community to expedite the dissemination of scientific material as soon as possible after acceptance. "Just Accepted" manuscripts appear in full in PDF format accompanied by an HTML abstract. "Just Accepted" manuscripts have been fully peer reviewed, but should not be considered the official version of record. They are citable by the Digital Object Identifier (DOI®). "Just Accepted" is an optional service offered to authors. Therefore, the "Just Accepted" Web site may not include all articles that will be published in the journal. After a manuscript is technically edited and formatted, it will be removed from the "Just Accepted" Web site and published as an ASAP article. Note that technical editing may introduce minor changes to the manuscript text and/or graphics which could affect content, and all legal disclaimers and ethical guidelines that apply to the journal pertain. ACS cannot be held responsible for errors or consequences arising from the use of information contained in these "Just Accepted" manuscripts.

ACS Publications

is published by the American Chemical Society. 1155 Sixteenth Street N.W., Washington, DC 20036

Published by American Chemical Society. Copyright © American Chemical Society. However, no copyright claim is made to original U.S. Government works, or works produced by employees of any Commonwealth realm Crown government in the course of their duties.

Operando Mapping of Li Concentration Profiles and Phase Transformations in Graphite Electrodes by MRI and NMR

Sergey A. Krachkovskiy,[1] Jamie M. Foster,[2] J. David Bazak,[1] Bruce J. Balcom,[3] and Gillian R. Goward[1*]

[1] Department of Chemistry & Chemical Biology, McMaster University, Hamilton, Ontario, Canada L8S 4L8.
[2] Department of Mathematics, University of Portsmouth, Portsmouth, Hampshire, UK PO1 3HF.
[3] Department of Physics, University of New Brunswick, Fredericton, New Brunswick, Canada E3B 5A3.

* Corresponding Author
Prof. Gillian R. Goward
Email: goward@mcmaster.ca
Phone: (905)-525-9140 x 24176
Fax: (905)-522-2509

Abstract

An innovative combined MRI and NMR methodology, which enables the visualization and spatially resolved quantification of the lithiation/delithiation process in porous Li-ion battery electrodes, in real time, is reported. We demonstrate that polarization of the thick graphite electrode correlates with the appearance of energy barriers during the graphite phase transformations and the resulting significant reduction of the lithium chemical diffusion, which must be addressed in any attempt at the fast charging of Li-ion batteries. It is also shown that a portion of the transported Li^+ is temporarily stored in the electrode surface film prior to its intercalation into graphite, indicating reversible lithium storage within the surface electrolyte interface. The inclusion of a short current reversal which could be considered as part of a *shaped* charging process, facilitates the complete lithiation of thick graphite electrodes; an attractive strategy for increasing usable cell capacities.

Introduction

The widespread deployment of Li-ion batteries (LIBs) for large-scale applications including automotive and grid-level energy storage requires both minimizing their cost and an increasing their energy density. This must be achieved without negatively affecting battery abuse tolerance, power performance, or durability. Utilization of thicker electrodes is one route towards achieving these goals, as it decreases the number of electrodes per cell, thus increasing the ratio of active material to current collectors. Previous studies indicate that a doubling of the electrode thickness can reduce the cell cost by 25%.[1] However, the lithium transport in such electrodes is impeded during battery operation even at moderate rates, leading to significant cell polarization and the under-utilization of its capacity.[2-4] It was suggested recently, comparing results of numerical simulations of cell voltage at different charge regimes with experimental data, that inadequate mass-transport through the electrolyte solution is the main factor limiting a thick electrode lithiation.[5] While fitting theoretically calculated voltage to measured ones yields modelling tools with good predictive power,[6-8] additional experiments for the validation of model predictions are desirable.

Graphite electrodes, which have been used in LIBs since their commercialization, are still the most relevant negative electrodes for electrified vehicle batteries.[9] Stoichiometric and thermodynamic stability, combined with good in-plane electronic conductivity, are important features of this material that make it attractive for LIB use. The Li intercalation into graphite is accompanied by a stage-like change in the average spacing of graphene planes, resulting in a rich phase diagram that displays distinct plateaus in a voltage vs. Li concentration plot.[10] The chemical diffusion coefficient of Li in graphite depends strongly on the amount of intercalated lithium. The appearance of distinct energy barriers at the end of each phase transformation cause an order of magnitude decrease in Li diffusivity when the transition from the stage 3 ($Li_{2/9}C_6$) to stage 2L ($Li_{1/3}C_6$) is complete.[11-12]

Phase nucleation and growth as a function of Li concentration is highly heterogeneous in typical electrode samples, making it difficult to analyse them by diffraction techniques. Color variations between the graphite lithiated to different stages were used to show, by digital optical microscopy, that there exists sharp boundaries between coloured areas during the galvanostatic charging of a graphite electrode at C/10 rate.[13] Well-resolved and significant differences in lithiation between various areas of an electrode were observed even when the Li-graphite cell was charged to

a potential of 2 mV vs. Li/Li^+. Color variations between particles provide qualitative information regarding lithium content in the electrode. Spectroscopic signatures, such as chemical shift differences between the dilute (1', 4, 3 and 2L) and the concentrated (2 and 1) stages of graphite lithiation in ^7Li nuclear magnetic resonance (NMR) spectra, can be used for more detailed study of the process.[14-16] Of these well-known stages of lithiated graphite, our discussion will focus on 2L, 2 and 1, with corresponding stoichiometries of $Li_{1/3}C_6$, $Li_{1/2}C_6$ and LiC_6, respectively. The *in situ* visualization and quantification of ion distributions inside electrochemical energy storage or power devices is also possible through other analytical techniques, such as neutron diffraction and scattering, X-ray absorption spectroscopy, and Mössbauer spectroscopy.[17-21] The main benefits of magnetic resonance method over alternative approaches arise from its non-destructive nature, and applicability to both crystalline and amorphous materials. Nevertheless, until recently, *in-situ* MRI was limited to monitoring species with favourable magnetic properties, e.g., electrolyte species or lithium dendrites.[22-23] The visualization of lithium intercalated into the active material particles of an electrode was significantly hampered by the extremely fast decay of the Li signal (transverse relaxation time $T_2 \leq 100$ μs), which can disappears before it is observed.[24] MRI imaging was recently reported for a lithium cobalt oxide // lithium titanate cell.[25] However, the fairly coarse (100 μm) spatial resolution of the images, coupled with an image acquisition time exceeding 3 hours, makes the applicability of the suggested technique to practical batteries questionable.

Here, for the first time, we report experimentally-determined lithium concentration profiles within a 300 μm thick graphite electrode during cell operation, which indeed reveals significant lithium concentration gradients and sharp boundaries between graphite areas lithiated to different stages. We combine ^7Li NMR spectroscopy with a single-point magnetic resonance imaging (SPMRI) technique, which provides images free from distortions caused by the static magnetic field inhomogeneity, susceptibility variations, and nuclear spin interactions.[26] The proposed method increases the spatial resolution to 50 μm, while substantially decreasing the data acquisition time. We map the spatial distribution of dilute and concentrated stages, and demonstrate that the polarization of the electrode occurs concurrently with the phase transformation in the graphite. Our results suggest that the detailes of Li transport not just in electrolyte but also in solid particles is highly important; thus, a more complex approach, than utilization of a constant solid-state diffusivity is needed for accurate modelling of battery (dis)charge. We show that a portion of the transported Li^+ is temporarily stored in the electrode surface film prior to its intercalation into

graphite. Its location can be identified by comparing experimentally obtained Li concentration profiles with those calculated based on porous electrode theory (PET). Finally, we demonstrate that insertion of a brief discharging step into the charging protocol mitigates the polarization of the electrolyte, enabling the electrode to overcome the Li diffusion barriers that appeared during graphite phase transformations and, in doing so, achieve a complete electrode lithiation.

Experimental

The composite graphite electrode consisted of graphite with an average particle diameter of 18 μm, electronically conductive Super P (Timcal) carbon filler and polyvinylidene fluoride (Kynar Arkema HSV900) binder in a mass ratio of 94.5:2.0:3.5. An active material – N-methyl pyrrolidone slurry (with 57:43 mass ratio) was prepared by mixing for a total of 10 minutes at 2000 rpm in an ARV-310 Thinky Mixer. Several periods of manual stirring with a spatula alternated with the mechanical stirring. Graphite electrodes with 300 μm thickness were solvent-cast onto a copper foil current collector using a doctor blade and air dried at 40°C overnight, followed by a temperature increase to 55°C and vacuum drying the next day, then a second temperature increase to 80°C and vacuum drying during a third day. The 4 mm diameter (5.32 mg graphite mass) composite electrode used in the electrophoretic NMR cell was cut from the Cu-supported electrode sheet.

A previously developed electrophoretic cell,[22, 27] was adopted for the present study (Fig. 1a). The cell consists of a polyether ether ketone (PEEK) cylindrical cell body with metallic lithium adhered to one and the copper foil supported graphite electrode to the other of the two copper current collectors hermetically sealed by means of PEEK Super Flangeless^{TM} HPLC fittings. The electrodes were separated by three glass microfiber filter membrane discs (#691, VWR Scientific Products), soaked in a 1 M $LiPF_6$ in ethylene carbonate (EC) : diethyl carbonate (DEC) (1:1 v/v) battery grade electrolyte solution (Sigma Aldrich). The inter-electrode spacing was ~200 μm. Cell assembly and filling with electrolyte solution were performed inside the Ar atmosphere of an MBRAUN glove box with 4.0 ppm oxygen and <0.1 ppm water contents. The graphite electrode and the separator were placed in the cell first, then the cell was filled with the electrolyte from the oposite side, and finally the lithium metal electrode was added. Note that part of the electrolyte solution was trapped within the case in the area behind the fitting, along the current collector and inside the threads of the cell body. The performance of the graphite//Li cell was tested with an Arbin BT 2000 battery cycler. In order to test the soundness of the cell design for electrocehmical constant

current cycling, the graphite electrode was first lithiated using a 20 μA current (corresponding to a C/100 rate) until a potential of 30 mV was reached, and was then held at that potential until the current decreased to 2 μA. The current was then reversed and the graphite was delithiated galvanostatically with a 20 μA current until the cell voltage reached 3.0 V (Fig. S1). The cell was then disassembled, cleaned and re-assembled with new electrodes, and inserted into the NMR spectrometer.

The *in-situ* NMR and MRI experiments were performed while applying a constant current of 45 μA (corresponding to a C/44 rate) to the cell, according to the following electrochemical testing protocol. A charging current was the first applied to the cell for 26 hours, until the potential reached the cut-off value of 2 mV vs. Li/Li^+. The direction of the current was then reversed during the ensuing 5 hours. Finally, the charging (intercalation) of the graphite electrode was then resumed for an additional 15 hours, until full lithiation of the graphite electrode was achieved. An Autolab PGStat 30 instrument operating in galvanostatic mode was used during the *in-situ* MRI and NMR experiments. Coaxial cables with grounded shields connected the cell to the potentiostat. An in-house low-pass LC filter (with a 2.3 MHz cut-off frequency) prevented additional noise from being picked-up by the NMR probe. This measurement configuration resulted in the same MRI signal-to-noise ratio irrespective of whether the coaxial cables were or were not connected to the cell. All experiments were carried out at 27°C using a Bruker Avance 300 NMR spectrometer equipped with a Diff50 gradient probe and a dual resonance 8 mm ^7Li / ^{19}F RF insert. The cell was positioned vertically inside the insert, with the B_0 field perpendicular to, and the B_1 field parallel to, the electrode surfaces, such that the copper current collectors did not prevent the penetration of the RF field into the active volume of the cell.

One-dimensional ^7Li images were acquired using a Centric Scan Single Point Ramped Imaging with T_1 Enhancement (CS SPRITE) pulse sequence which inherits all the advantages of SPMRI while also significantly decreasing the image collection time.[28-29] The linear gradient ramps were constructed with 64 equidistant points for each half k-space sequence, ranging in magnitude up to a field gradient of 1,760 $G \cdot cm^{-1}$. The excitation at each step was achieved with a 0.7 μs broadband pulse (which corresponds to a tip angle (θ) of 3°); 10 free induction decay (FID) points were collected following the excitation pulse and summed as described by Halse et al.[28] to generate the image with a 30 μs phase-encoding time (t_p) and 0.8 μs dwell time. The spatial resolution of the reconstructed images is 50 μm. In order to achieve an acceptable signal-to-noise ratio, 4096 scans

were averaged for each image collected during the cell operation, with a recycling delay of 0.9 s, resulting in a total data collection time of 2 hours per image.

Single pulse *in situ* ^{7}Li NMR spectra were also acquired after each image acquisition, using an 11 μs excitation pulse, 64 scans and an 8.5 s relaxation delay, amounting to a 9 min total experiment time. Note that the acqusition time for these ^{7}Li NMR spectra represents only 8% of the acquisition time for the MR images. Spectral deconvolution was performed using the dmfit2015 software.[30]

Simulations were carried out using a porous electeode theory model of the half cell. This approach, originally proposed by Fuller,[31] was formalized by Richardson et al. via the multiple scales method.[32] The latter allows the systematic simplification of a set of equations posed on a geometry with two or more distinct length scales, and has been used to generate simplified electrochemical models[33-34] and solid mechanical models for Li-ion cells.[35] A system of coupled partial differential equations was solved using a bespoke numerical method in MATLAB that uses finite differences, control volumes and adaptive time steps. A more in-depth description of the model formulation and its numerical solution are given in the Supplementary Information (SI).

Results and Discussion

The combination of ^{7}Li in operando MRI and interleaved ^{7}Li NMR spectroscopy allow us to profile the lithiation of the graphite electrode in real time during the cell operation, establishing both speciation and quantitative concentration simultaneously. Tracking the formation of the lithiated stages of graphite spectroscopically provides key insights into the reasons for the observed concentration profiles. Initially, only ^{7}Li signals from $LiPF_6$ in the electrolyte solution (at -2.8 ppm, Fig. 1 d) and from lithium metal electrode (263 ppm, not shown) are visible in the NMR spectrum of the freshly assembled cell. The electrolyte solution is located between cell coordinates 300 and 500 μm, while the lithium electrode is between 500 and 700 μm in the image (Fig. 1 c). We could not detect the ^{7}Li MRI signal from the electrolyte filling the pores in the graphite (cell coordinates 0 – 300 μm) due to the low porosity of the electrode and the fact that the recycling delay of 0.9 seconds used in the experiment is optimized for acquiring signal from the fast-relaxing intercalated lithium (longitudinal relaxation time $T_1 \approx 100$ ms), but not from the lithium in the electrolyte solution or in the solid electrolyte interface (SEI) ($T_1 \approx 2$ s).[36] It should also be noted that only the surface of the lithium metal disk can be observed by NMR, due to the limited penetration of the electromagnetic

field into conductors.[37] The ^{7}Li NMR signal corresponding to the electrolyte in the separator shifts from -2.8 to 8.4 ppm during the first four hours of the experiment due to the change of graphite magnetic susceptibility (see SI for slice-selective NMR spectra and detailed peak assignment). Intensity of the Li-metal signal does not change during the same time, meaning that the RF field or Q-factor of the probe do not vary as the intercalation proceeds.

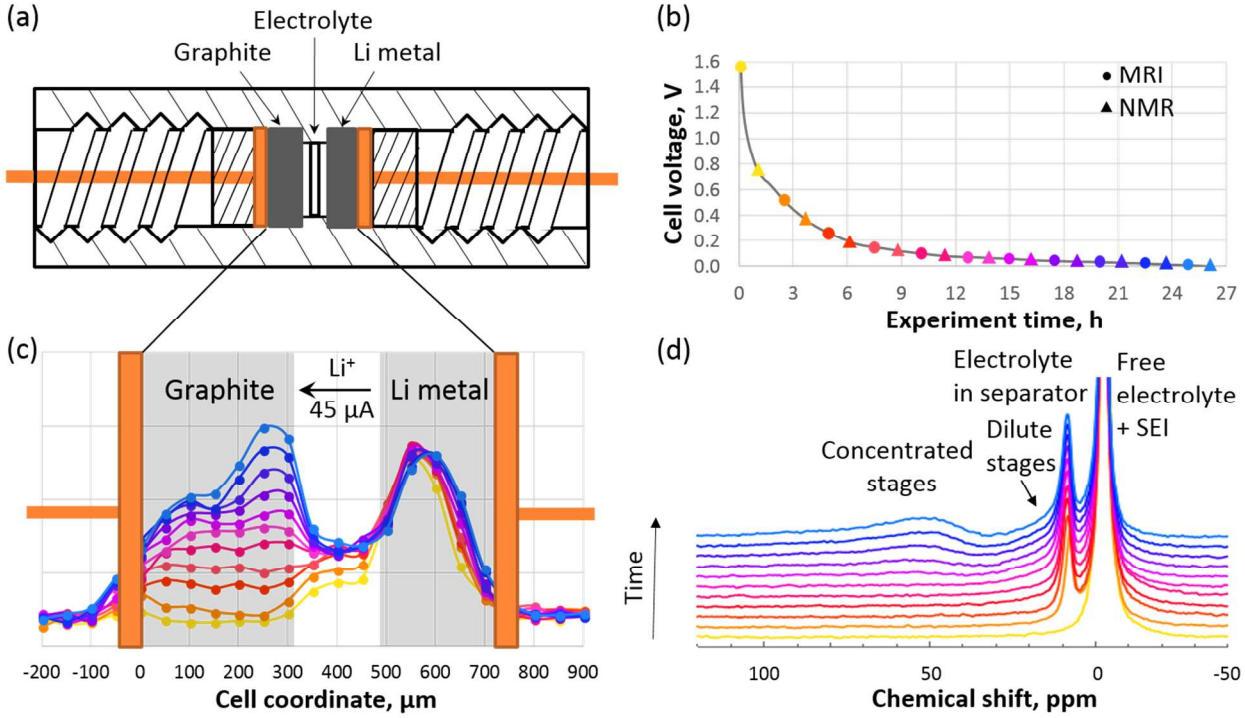

Figure 1. *(a) Schematic representation of the in-situ cell; (b) voltage vs. time curve for graphite during the first charging step; (c) axial ^{7}Li MR images; and (d) ^{7}Li NMR spectra collected during charging. The circles of a given color in panel (b) correspond to the curves with same color from panel (c), while the triangles correspond to the curves with the same colors from panel (d).*

The formation of the dilute stages during the Li intercalation into graphite can be detected by the simultaneous uniform increase in the image intensity throughout the electrode's axial cross-section and by the growth in intensity of the broad signal at ~10 ppm (see SI for an example spectrum deconvolution).[14] The graphite lithiation process is almost uniform throughout the 300 µm electrode during the first 10 hours of the experiment, until the dilute stages begin to transform into concentrated stages. The latter can be identified by their spectroscopic signature, namely a broad resonance at ~50 ppm in the ^{7}Li NMR spectrum. A key observation is that the sloped concentration profile emerges at the same time as the appearance of the higher frequency ^{7}Li NMR signal. The images representing concentration profiles show that the concentration continues to increase in

graphite near the interface between the electrode and the electrolyte-filled separator, while the Li content in the electrode volume near the current collector stops increasing. Finally, the electrode polarization reaches such an extent that a negative potential versus Li metal would be needed for continuing the cell charging past 26 hours, the moment when the cell potential reaches the 2 mV cut-off value. Note that only 59% of the graphite theoretical capacity is reached at this point, even though the intercalation rate is 10 to 100 times smaller than that typical for practical LIBs.

To quantify the speciation within the electrode, we construct a series of relationships that link the lithium concentration to the ^{7}Li *image* intensity, to relaxation properties of the nuclei in each phase, and to the integrated *spectral* intensity for the concentrated and dilute species. The local signal intensity at any point in the image can be expressed as:

$$S = M_0 e^{-t_p / T_2^*} \sin\theta \qquad (1a)$$

where M_0 is the net magnetization, which is proportional to the total number of lithium nuclei present in the immediate vicinity of the point, t_p is the spatial encoding time of the MRI experiment, and θ is the tip angle of the magnetization caused by the applied RF pulse.[38] Since the ^{7}Li nuclei in the dilute and concentrated stages of graphite have different transverse relaxation times, Eqn. 1a can be rewritten as:

$$S = kN(p_d e^{-t_p / T_{2,d}^*} + p_c e^{-t_p / T_{2,c}^*}) \qquad (1b)$$

with k the transverse magnetization ($M_0 \sin\theta$) divided by the number of lithium atoms (N). Further, p_c and p_d are the fractions of the intercalated lithium present in the concentrated and dilute stages of graphite respectively, determined from the relative integrated intensities of the corresponding NMR signals (Table 1). $T_{2,c}^*$ and $T_{2,d}^*$ are the transverse relaxation times, which are the inverse of the width at half height of the corresponding NMR lines measured in Hz (Table 1).

Table 1. *Relative fractions of ^{7}Li nuclei in the dilute and concentrated stages of the Li-intercalated graphite and the corresponding ^{7}Li transverse NMR relaxation times (T_2^*).*

Experiment Time, h	Dilute Stages		Concentrated Stages	
	p_d, a.u.	$T_{2,d}^*$, ms	p_c, a.u.	$T_{2,c}^*$, ms
3.75	1.00	0.10 ± 0.01	–	–
6.25	1.00	0.10 ± 0.01	–	–
8.75	1.00	0.10 ± 0.01	–	–
11.25	1.00	0.10 ± 0.01	–	–
13.75	0.80 ± 0.02	0.11 ± 0.01	0.20 ± 0.01	0.045 ± 0.005

16.25	0.74 ± 0.02	0.11 ± 0.01	0.26 ± 0.01	0.056 ± 0.006
18.75	0.66 ± 0.01	0.11 ± 0.01	0.34 ± 0.01	0.061 ± 0.006
21.25	0.54 ± 0.01	0.11 ± 0.01	0.46 ± 0.01	0.063 ± 0.006
23.75	0.48 ± 0.01	0.12 ± 0.01	0.52 ± 0.02	0.065 ± 0.006
26.25	0.36 ± 0.01	0.13 ± 0.01	0.64 ± 0.02	0.065 ± 0.006

The evolution of the kN product over the duration of the experiment (calculated using Eqn. 1b) is displayed in Figure 2. A kN value error was estimated as 3% using a Monte-Carlo analysis with 100 independent calculations based on randomly varied within standard deviations parameters p_c, p_d, $T^*_{2,c}$ and $T^*_{2,d}$. The data points between hours 2.5 and 12.5 of the experiment display a linear dependence on time (R^2 = 0.997, slope = 2.77). The fact that this line crosses the y-axis below zero means that not all the transported Li^+ intercalates into the graphite at the beginning of its lithiation. Rather, a portion of the lithium is consumed in the electrochemical reduction of electrolyte solution components, to form the SEI. The slope of the data changes markedly to 1.90 after 12.5 hours (R^2 = 1.000), indicating a second stage of the side reactions and further SEI growth.[18, 38] It is reasonable to assume that all Li^+ cations (ΔN) carried by the electric current (I) accumulate in the graphite electrode during the period of time (Δt) of the first 10 hours of linear response so that

$$\Delta N = \frac{I\Delta t}{F} \qquad (2)$$

where F is the Faraday constant. One can determine the coefficient k from the data and then transform the image intensity into the amount of lithium intercalated into graphite. Even though the NMR signal of the SEI is hidden under the much higher peak of the free electrolyte, the amount of lithium consumed in parasitic reactions can be indirectly obtained from the deviation of the data points on Fig. 2 from the line drawn through zero with the same slope. For example, only 66% of the transferred lithium is intercalated into the graphite during first 2.5 hours. After 25 hours 20% of the total lithium deposited at the negative electrode was consumed in SEI formation and growth.

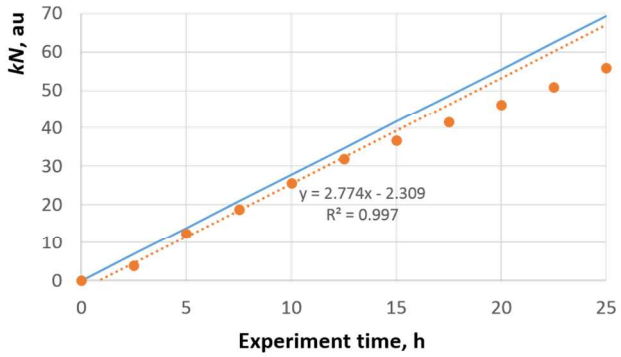

Figure 2. *Evolution of the kN product (orange dots) over the duration of the experiment. The dashed orange line indicates the linear-response region between 2.5 and 12.5 hours, the solid blue line indicates the total amount of lithium transferred.*

Optical reflectance imaging of a single crystal graphite electrode revealed that Li intercalation into graphite occurs homogeneously during the dilute stages of lithiation, while the further nucleation toward the concentrated stages happens on the boundary of the particle.[39] Moreover, stage 1 (LiC_6) appears on the surface of the particle almost immediately after stage 2 ($Li_{1/2}C_6$) forms, meaning that the system is out of equilibrium, forming steep Li concentration gradients at the edge. We can utilize this observation in order to extract the distribution of dilute and concentrated stages through the electrode from the MRI/NMR data. We divide the 300 μm thick graphite electrode into six slices of 50 μm, as per the spatial resolution of the MRI experiment. Then we check with Eqn. 1 if the image intensity in the slice can be obtained with dilute stages only (lithium concentration in these stages should be no more than 1/3 of the maximum possible concentration c_{max}). If not, then we assume that the edge of graphite particles are occupied by the concentrated stage with average concentration $\alpha\, c_{max}$ (with $\alpha > 1/3$) and total volume of V_c, while the core of the particles are filled with the saturated dilute stage $Li_{1/3}C_6$ (Eqn. 3, where V is the volume of active material in the slice, see SI).

$$S = kc_{max}\left(\frac{1}{3}(V - V_c)e^{-\frac{t_p}{T^*_{2,d}}} + aV_c e^{-\frac{t_p}{T^*_{2,c}}}\right) \qquad (3)$$

α is adjusted to match the ratio of the total amount of lithium in the dilute and the concentrated stages to the same ratio extracted from NMR spectra (p_d/p_c).

The quantitative, spatially resolved evaluation of the lithiated graphite species as a function of charge is shown in Fig. 3. Note, that bars on the figure represent amount of lithium in concentrated and dilute stages (x in Li_xC_6) in each slice of the electrode. Volumes occupied by each stage in graphite particles are shown as a disk diagrams for the slices where both concentrated and dilute phases coexist, demonstrating that the boundary between stages moves from the edge toward the center of the particle. Initially, the decreasing equilibrium overpotential curve (Fig 1b) encourages a roughly equal lithiation of all graphite particles causing the flat concentration profile during the first 10 hours of the experiment. If a certain particle becomes more lithiated than those around it, then its overpotential decreases, so that insertion into it is no longer favorable. However, once a value of the x near 0.22 is reached (Fig. 3, 10.0 hours), which occurs roughly simultaneously

throughout the electrode, the graphite reaches the 100 mV plateau and transformation from $Li_{2/9}C_6$ to $Li_{1/3}C_6$ and then to $Li_{1/2}C_6$ begins. The incentive for the lithium to fill uniformly across the breadth of the electrode has now been removed by the flattening of the overpotential. Electrolyte polarization[22] means that the region closest to the separator (slice #6, Fig. 3) is more Li-rich than that near the current collector. Thus, insertion into particles in this slice is favored. A drastic decrease in the solid-state diffusivity occurs at x = 1/3.[11] At this point a relatively large salt concentration in the electrolyte is required to overcome the diffusion barrier and continue the insertion of Li into the active material particles. Therefore, phase transformation starts in slice #6 and proceeds until its completion (Fig.3, 17.5 hours) followed by an appearance of the next energy barrier.[11] Then, the reaction front moves towards the deeper regions of the electrode nearer to the separator, as reveal in the concentration profile. At the point when the cell reaches the 2 mV cut-off potential, the layer of the graphite electrode closest to the separator is highly lithiated (to x = 0.77, 25.0 hours), while the slice closest to the current collector are at only x = 0.30. This is a clear indication of a potential limitation of thick graphite electrode design.

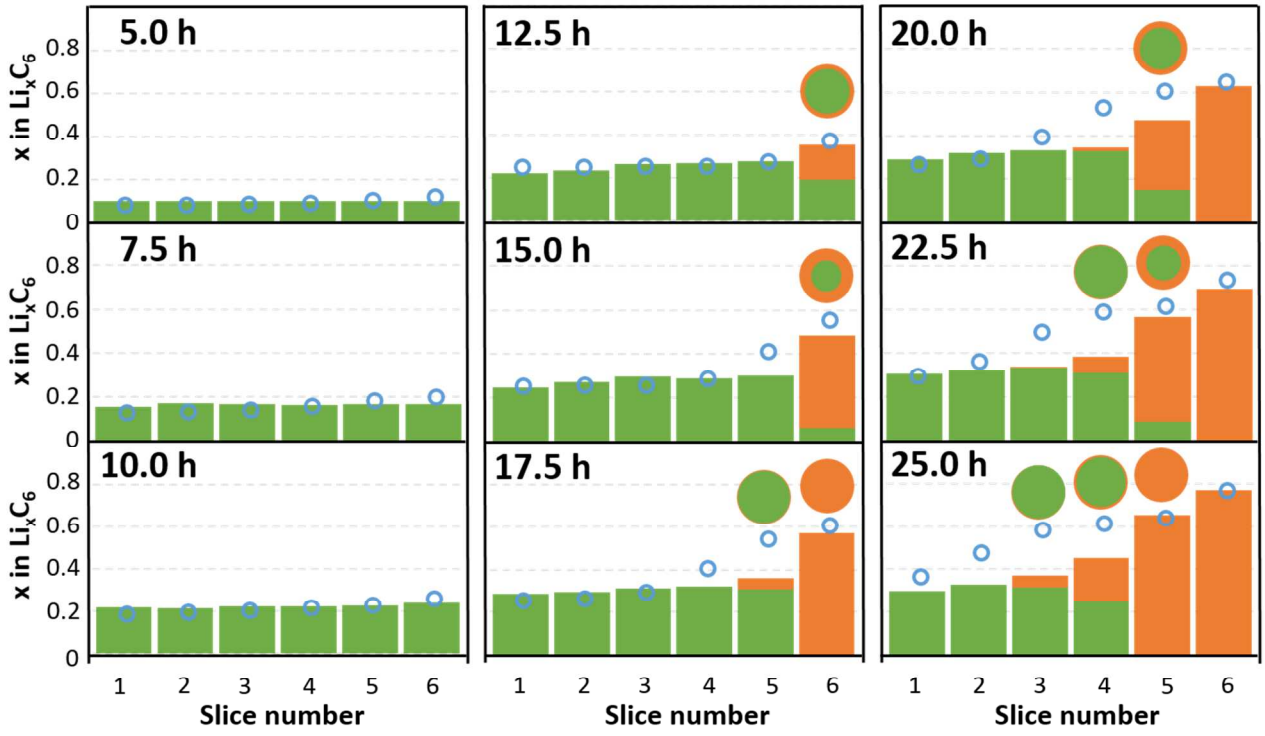

Figure 3. *Lithium concentration profiles determined from the MR images and the transverse relaxation times extracted from NMR spectra using equations (1) – (2) displaying the relative populations of concentrated (orange) and dilute (green) stages. Slice 1 is nearest to the current collector, as in Figure 1c. The blue circles represent lithium concentration in the slices obtained*

from modelling. The disk diagrams demonstrate volume distribution of concentrated and dilute stages in graphite particles.

We simulated lithiation of the graphite electrode using PET with solid-state Li diffusion coefficient distribution vs. x value reported by Levi *et al.*[11] (see SI) in order to discern how the measured lithium concentration profiles correlate with the theoretical concentrations. A favorable correlation is observed (blue dots in Fig. 3), with the exception that PET does not consider SEI formation reactions. The amount of Li^+ in the electrolyte is conserved in the model, and, consequently all the Li^+ leaving the electrolyte enters the graphite in the form of Li. In other words, PET has a rate of lithium intercalation shown by the blue line in Fig. 2. Comparing modelling and experimental results, we can identify the electrode regions where the side reactions take place. The most significant deviations are observed for the layers of graphite which have not overcome the critical amount of lithium associated with the phase transformation and the diffusion barrier ($x \approx 1/3$), and which are close enough to the separator to have a sufficient source of Li^+ cations. As a result, lithium is trapped on the surface of the particles there, participating in side-reactions leading to the growth of SEI and to capacity fade.

The formation of such a steep concentration gradient within the thick graphite electrode clearly poses a problem to its utilization. In order to remedy this, we propose a *shaped charging process*, as follows. The lithium salt concentration in the electrolyte regions closer to the current collector must increase, to facilitate further lithiation of the graphite particles in that part of the electrode. This can be achieved either by reducing electric current (e.g. by switching the charging protocol to potentiostatic mode) and allowing the salt concentration gradient in the electrolyte to slowly relax, or by a relatively brief current reversal, i.e., by briefly discharging the cell. During this discharging over 5 hours , the lithium-rich graphite in the vicinity of the separator releases lithium ions into the electrolyte solution in order to decrease its overpotential and reach an equilibrium with the particles that are closer to the current collector. The signal from the concentrated stages decreases in the NMR spectrum collected after 5 hours of the delithiation at 45 μA (Figs. 4a and 5a) and the T_2^* relaxation time (measured separately from the 1D ^{7}Li NMR spectrum) increases, becoming comparable to that of the dilute stages (0.1 ms). Lithium ions released from the graphite migrate under the applied electric field through the separator towards the Li electrode, where they deposit and form a mossy structure with significantly higher surface area, which causes an increase of the Li signal in the corresponding image region. Furthermore, a lithium salt concentration gradient is established in the electrolyte solution within the porous graphite electrode, causing a

diffusive flux that counters the current flow and extends deeper into the electrode. Lithium ions will therefore move towards the current collector (i.e., the back of the electrode), creating conditions that are favourable for lithium insertion into the graphite particles there. Consistent with this scenario, the image intensity increases in that region of the electrode (Fig. 4b, c). This implies that the increase of the lithium salt concentration in the electrolyte solution in the deeper region of the electrode, due to the reversal of the current, serves as an intermediate step to support overcoming of the solid-state diffusivity barrier for lithium intercalated into graphite particles and to form a dense stage shell on their surface. Note that, besides the lithium redistribution within the graphite during the discharging, the total amount of lithium in the electrode is 8% higher than the expected amount, based on the applied current. To compensate the charge carried by the electrons through the outer circuit, 37% of lithium consumed in the SEI at the end of the lithiation (deviation between measured and calculated profiles on Fig. 3, 25 hours) must have been released and consequently intercalated into the graphite. This hypothesis agrees with the observation that the SEI on a graphite electrode is significantly thinner at the end of discharge than at the end of charge, during first three cycles of a LIB [40] providing an additional source of Li and increasing electrode capacity.[41-42]

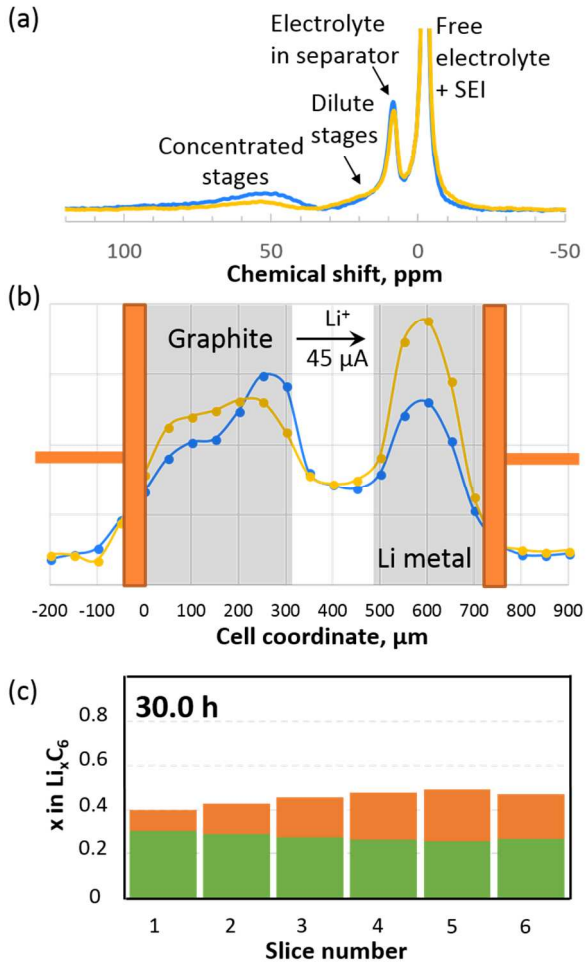

Figure 4. *(a) ^{7}Li NMR data collected at the end of charging (blue) and after 5 hours of discharging (yellow) at 45 µA current. (b) ^{7}Li MR images acquired immediately before collecting the spectra shown in panel (a). (c) Li concentration profile in the graphite electrode after 5 hours of its delithiation, determined from the corresponding spectrum and image from panels (a) and (b), respectively.*

After this current reversal, a higher overall degree of graphite lithiation can be achieved by driving current from Li-metal to the graphite (Fig. 5). A significant growth of Li-rich stages throughout the electrode becomes apparent, concomitant with the disappearance of the dilute phase from the NMR spectrum. Lithiation occurs now without any significant polarization, as manifested both in the lithium concentration profiles (which display more slices saturated with lithium) as well as cell potential. In addition, the derivative of the kN product with respect to time is 2.84 after the current reversal, differing by less than 3% from its value during the time interval from 2.5 to 12.5 hours (Fig.5a). The dense shell, formed on the surface of graphite particles during current reversal, provides a sufficient concentration gradient to drive diffusion toward the core of the particles. Based on this data we infer that the boundary of $Li_{1/3}C_6$ phase with extremely low Li solid-state diffusion is

now within the particles and is not exposed to the electrolyte, therefore all the transferred lithium intercalates into graphite without consumption in parasitic reactions.

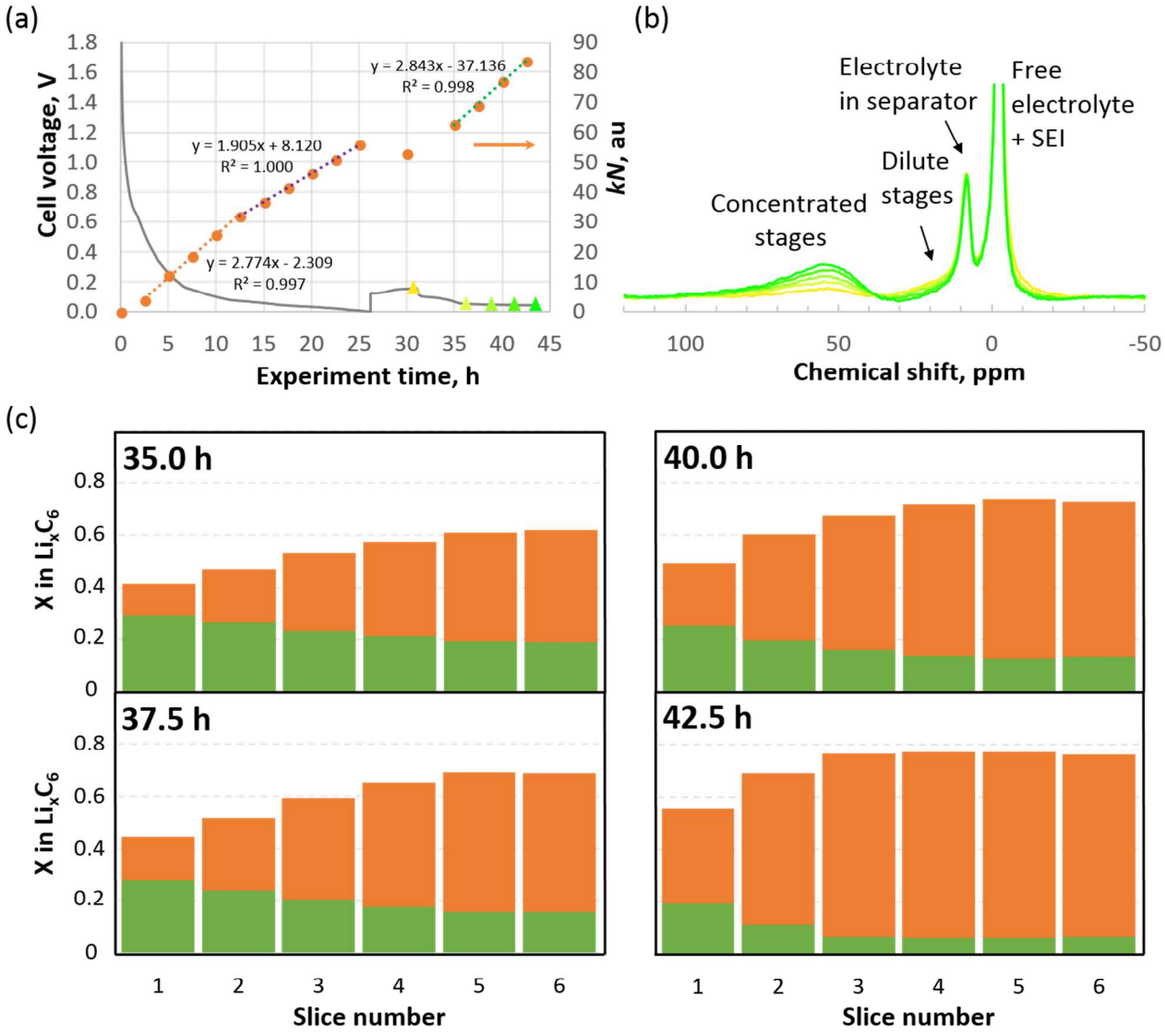

Figure 5. *(a) Cell voltage as function of time through the entire electrochemical test (grey line), and evolution of the kN product over the duration of the experiment (brown dots). The dashed lines and the fit parameters indicate the linear-response regions (b) ^{7}Li NMR spectra collected after the conclusion of the deintercalation step and during the subsequent resumption of intercalation (prior to the acquisition of the MR images used for generating the concentration profiles). The colors of the spectra correspond to the colored triangles on the voltage profile from panel a. (c) Lithiation profiles of the graphite electrode during the second galvanostatic charging step with 45 μA current.*

Conclusions

Using magnetic resonance techniques we were able to visualize and quantify the lithium distribution within a graphite electrode during operation; we found that the electrode polarization correlates with phase transformations of the graphite; unfavorable Li dynamics during these transformations leads to side reactions on the particles interface. The effect of the side reactions can be minimized with a proper charging protocol.

Supporting information

Detailed description of the electrophoretic cell performance, *in situ* ^{7}Li slice-selective NMR spectra, example of the ^{7}Li NMR spectrum deconvolution, and in-depth description of the porous electrode theory model formulation and its numerical solution. This material is available free of charge via the Internet at http://pubs.acs.org.

Acknowledgments

The authors are grateful to Dr. Ion C. Halalay and Dr. Nicole D. Ellison for the provided graphite samples and for helpful discussions regarding ion transport in Li-ion batteries, and thank Dr. Bryce MacMillan and Dr. Klaus Zick for discussions regarding MRI techniques. They also acknowledge funding through the NSERC Strategic grant program, GM of Canada and Bruker BioSpin Canada.

References:

1. Patry, G.; Romagny, A.; Martinet, S.; Froelich, D. Cost Modelling of Lithium-Ion Battery Cells for Automotive Applications. *Energy Sci. & Eng.* **2015,** *3*, 71-82.

2. Buqa, H.; Goers, D.; Holzapfel, M.; Spahr, M. E.; Novák, P. High Rate Capability of Graphite Negative Electrodes for Lithium-Ion Batteries. *J. Electrochem. Soc.* **2005,** *152*, A474-A481.

3. Singh, M.; Kaiser, J.; Hahn, H. Thick Electrodes for High Energy Lithium Ion Batteries. *J. Electrochem. Soc.* **2015,** *162*, A1196-A1201.

4. Danner, T.; Singh, M.; Hein, S.; Kaiser, J.; Hahn, H.; Latz, A. Thick Electrodes for Li-Ion Batteries: A Model Based Analysis. *J. Power Sources* **2016,** *334*, 191-201.

5. Gallagher, K. G.; Trask, S. E.; Bauer, C.; Woehrle, T.; Lux, S. F.; Tschech, M.; Lamp, P.; Polzin, B. J.; Ha, S.; Long, B., et al. Optimizing Areal Capacities through Understanding the Limitations of Lithium-Ion Electrodes. *J. Electrochem. Soc.* **2015,** *163*, A138-A149.

6. Doyle, M.; Fuentes, Y. Computer Simulations of a Lithium-Ion Polymer Battery and Implications for Higher Capacity Next-Generation Battery Designs. *J. Electrochem. Soc.* **2003,** *150*, A706-A713.

7. Dargaville, S.; Farrell, T. W. Predicting Active Material Utilization in $LiFePO_4$ Electrodes Using a Multiscale Mathematical Model. *J. Electrochem. Soc.* **2010,** *157*, A830-A840.

8. Srinivasan, V.; Newman, J. Design and Optimization of a Natural Graphite/Iron Phosphate Lithium-Ion Cell. *J. Electrochem. Soc.* **2004,** *151*, A1530-A1538.

9. Blomgren, G. E. The Development and Future of Lithium Ion Batteries. *J. Electrochem. Soc.* **2016,** *164*, A5019-A5025.

10. Dahn, J. R. Phase Diagram of Li_xC_6. *Phys. Rev. B* **1991,** *44*, 9170-9177.

11. Levi, M. D.; Wang, C.; Markevich, E.; Aurbach, D.; Chvoj, Z. Noteworthy Electroanalytical Features of the Stage 4 to Stage 3 Phase Transition in Lithiated Graphite. *J. Solid State Electrochem.* **2003,** *8*, 40-43.

12. Baker, D. R.; Verbrugge, M. W. Intercalate Diffusion in Multiphase Electrode Materials and Application to Lithiated Graphite. *J. Electrochem. Soc.* **2012,** *159*, A1341-A1350.

13. Harris, S. J.; Timmons, A.; Baker, D. R.; Monroe, C. Direct In Situ Measurements of Li Transport in Li-Ion Battery Negative Electrodes. *Chem. Phys. Lett.* **2010,** *485*, 265-274.

14. Letellier, M.; Chevallier, F.; Morcrette, M. In Situ ^{7}Li Nuclear Magnetic Resonance Observation of the Electrochemical Intercalation of Lithium in Graphite; 1st Cycle. *Carbon* **2007,** *45*, 1025-1034.

15. Zaghib, K., Tatsumia, K., Sawadaa, Y., Higuchia, S., Abeb, H., Ohsaki, T. ^{7}Li-NMR of Well-Graphitized Vapor-Grown Carbon Fibers and Natural Graphite Negative Electrodes of Rechargeable Lithium-Ion Batteries. *J. Electrochem. Soc.* **1999,** *146*, 2784-2793.

16. Chevallier, F.; Poli, F.; Montigny, B.; Letellier, M. In Situ ^{7}Li Nuclear Magnetic Resonance Observation of the Electrochemical Intercalation of Lithium in Graphite: Second Cycle Analysis. *Carbon* **2013,** *61*, 140-153.

17. Ebner, M.; Marone, F.; Stampanoni, M.; Wood, V. Visualization and Quantification of Electrochemical and Mechanical Degradation in Li Ion Batteries. *Science* **2013,** *342*, 716-720.

18. Liu, D. X.; Wang, J.; Pan, K.; Qiu, J.; Canova, M.; Cao, L. R.; Co, A. C. In Situ Quantification and Visualization of Lithium Transport With Neutrons. *Angew. Chem. Int. Ed. Engl.* **2014,** *53*, 9498-9502.

19. Strobridge, F. C.; Orvananos, B.; Croft, M.; Yu, H.-C.; Robert, R.; Liu, H.; Zhong, Z.; Connolley, T.; Drakopoulos, M.; Thornton, K., et al. Mapping the Inhomogeneous Electrochemical Reaction Through Porous $LiFePO_4$-Electrodes in a Standard Coin Cell Battery. *Chem. Mater.* **2015,** *27*, 2374-2386.

20. Siegel, J. B.; Lin, X.; Stefanopoulou, A. G.; Hussey, D. S.; Jacobson, D. L.; Gorsich, D. Neutron Imaging of Lithium Concentration in LFP Pouch Cell Battery. *J. Electrochem. Soc.* **2011,** *158*, A523-A529.

21. Conte, D. E.; Mouyane, M.; Stievano, L.; Fraisse, B.; Sougrati, M. T.; Olivier-Fourcade, J.; Willmann, P.; Jordy, C.; Artus, M.; Cassaignon, S., et al. A Combined Mössbauer Spectroscopy and X-Ray Diffraction Operando Study of Sn-Based Composite Anode Materials for Li-Ion Accumulators. *J Solid State Electrochem.* **2012,** *16*, 3837-3848.

22. Krachkovskiy, S. A.; Bazak, J. D.; Werhun, P.; Balcom, B. J.; Halalay, I. C.; Goward, G. R. Visualization of Steady-State Ionic Concentration Profiles Formed in Electrolytes during Li-Ion Battery Operation and Determination of Mass-Transport Properties by In Situ Magnetic Resonance Imaging. *J. Am. Chem. Soc.* **2016,** *138*, 7992-7999.

23. Chang, H. J.; Ilott, A. J.; Trease, N. M.; Mohammadi, M.; Jerschow, A.; Grey, C. P. Correlating Microstructural Lithium Metal Growth with Electrolyte Salt Depletion in Lithium Batteries Using ^{7}Li MRI. *J. Am. Chem. Soc.* **2015,** *137*, 15209-15216.

24. Salager, E.; Sarou-Kanian, V.; Sathiya, M.; Tang, M.; Leriche, J.-B.; Melin, P.; Wang, Z.; Vezin, H.; Bessada, C.; Deschamps, M., et al. Solid-State NMR of the Family of Positive Electrode Materials $Li_2Ru_{1-y}Sn_yO_3$ for Lithium-Ion Batteries. *Chemistry of Materials* **2014,** *26*, 7009-7019.

25. Tang, M.; Sarou-Kanian, V.; Melin, P.; Leriche, J. B.; Menetrier, M.; Tarascon, J. M.; Deschamps, M.; Salager, E. Following Lithiation Fronts in Paramagnetic Electrodes With In Situ Magnetic Resonance Spectroscopic Imaging. *Nature Commun.* **2016,** *7*, article 13284.

26. Gravina, S.; Cory, D. G. Sensitivity and Resolution of Constant-Time Imaging. *Journal of Magnetic Resonance, Series B* **1994,** *104*, 53-61.

27. Bazak, J. D.; Krachkovskiy, S. A.; Goward, G. R. Multi-Temperature In Situ Magnetic Resonance Imaging of Polarization and Salt Precipitation in Lithium-Ion Battery Electrolytes. *J. Phys. Chem. C* **2017,** *121*, 20704-20713.

28. Halse, M.; Rioux, J.; Romanzetti, S.; Kaffanke, J.; MacMillan, B.; Mastikhin, I.; Shah, N. J.; Aubanel, E.; Balcom, B. J. Centric Scan SPRITE Magnetic Resonance Imaging: Optimization of SNR, Resolution, and Relaxation Time Mapping. *J. Magn. Reson.* **2004,** *169*, 102-117.

29. Romanenko, K.; Forsyth, M.; O'Dell, L. A. New Opportunities for Quantitative and Time Efficient 3D MRI of Liquid and Solid Electrochemical Cell Components: Sectoral Fast Spin Echo and SPRITE. *J. Magn. Reson.* **2014,** *248*, 96-104.

30. Massiot, D.; Fayon, F.; Capron, M.; King, I.; Le Calvé, S.; Alonso, B.; Durand, J.-O.; Bujoli, B.; Gan, Z.; Hoatson, G. Modelling One- and Two-Dimensional Solid-State NMR Spectra. *Magn. Reson. Chem.* **2002,** *40*, 70-76.

31. Fuller, T. F.; Doyle, M.; Newman, J. Simulation and Optimization of the Dual Lithium Ion Insertion Cell. *J. Electrochem. Soc.* **1994,** *141*, 1-10.

32. Richardson, G.; Denuault, G.; Please, C. P. Multiscale Modelling and Analysis of Lithium-Ion Battery Charge and Discharge. *J. Eng. Math.* **2011,** *72*, 41-72.

33. Gully, A.; Liu, H.; Srinivasan, S.; Sethurajan, A. K.; Schougaard, S.; Protas, B. Effective Transport Properties of Porous Electrochemical Materials -- A Homogenization Approach. *J. Electrochem. Soc.* **2014,** *161*, E3066-E3077.

34. Foster, J. M.; Gully, A.; Liu, H.; Krachkovskiy, S.; Wu, Y.; Schougaard, S. B.; Jiang, M.; Goward, G.; Botton, G. A.; Protas, B. Homogenization Study of the Effects of Cycling on the Electronic Conductivity of Commercial Lithium-Ion Battery Cathodes. *J. Phys. Chem. C* **2015,** *119*, 12199-12208.

35. Foster, J. M.; Huang, X.; Jiang, M.; Chapman, S. J.; Protas, B.; Richardson, G. Causes of Binder Damage in Porous Battery Electrodes and Strategies to Prevent It. *J. Power Sources* **2017,** *350*, 140-151.

36. Letellier, M.; Chevallier, F.; Béguin, F.; Frackowiak, E.; Rouzaud, J.-N. The First In Situ ^{7}Li NMR Study of the Reversible Lithium Insertion Mechanism in Disorganised Carbons. *J. Phys. Chem. Solids* **2004,** *65*, 245-251.

37. Ilott, A. J.; Chandrashekar, S.; Klockner, A.; Chang, H. J.; Trease, N. M.; Grey, C. P.; Greengard, L.; Jerschow, A. Visualizing Skin Effects in Conductors With MRI: ^{7}Li MRI Experiments and Calculations. *J. Magn. Reson.* **2014,** *245*, 143-149.

38. Halse, M.; Goodyear, D. J.; MacMillan, B.; Szomolanyi, P.; Matheson, D.; Balcom, B. J. Centric Scan SPRITE Magnetic Resonance Imaging. *J. Magn. Reson.* **2003,** *165*, 219-229.

39. Guo, Y.; Smith, R. B.; Yu, Z.; Efetov, D. K.; Wang, J.; Kim, P.; Bazant, M. Z.; Brus, L. E. Li Intercalation into Graphite: Direct Optical Imaging and Cahn-Hilliard Reaction Dynamics. *J. Phys. Chem. Lett.* **2016,** *7*, 2151-2156.

40. Bryngelsson, H.; Stjerndahl, M.; Gustafsson, T.; Edström, K. How Dynamic is The SEI? *J. Power Sources* **2007,** *174*, 970-975.

41. Hu, Y. Y.; Liu, Z.; Nam, K. W.; Borkiewicz, O. J.; Cheng, J.; Hua, X.; Dunstan, M. T.; Yu, X.; Wiaderek, K. M.; Du, L. S., et al. Origin of Additional Capacities in Metal Oxide Lithium-Ion Battery Electrodes. *Nature Mater.* **2013,** *12*, 1130-1136.

42. Rezvani, S. J.; Gunnella, R.; Witkowska, A.; Mueller, F.; Pasqualini, M.; Nobili, F.; Passerini, S.; Cicco, A. D. Is the Solid Electrolyte Interphase an Extra-Charge Reservoir in Li-Ion Batteries? *ACS Appl. Mater. Interfaces* **2017,** *9*, 4570-4576.

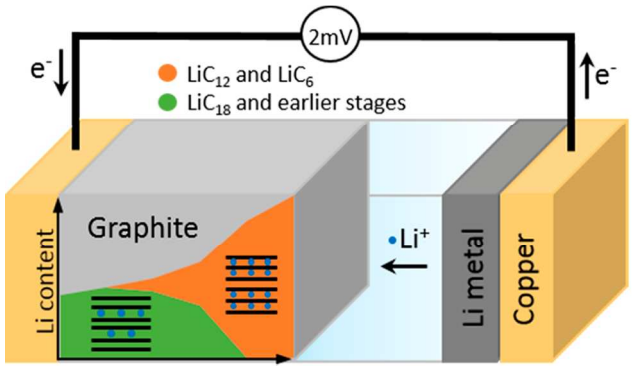
2mV
e-
e-
LiC12 and LiC6
LiC18 and earlier stages
Graphite
Li content
Li+
Li metal
Copper